The Impact of ENSO on Atmospheric Intraseasonal Variability as Inferred from Observations and GCM Simulations

CHI-YUNG TAM*

Atmospheric and Oceanic Sciences Program, Princeton University, Princeton, New Jersey

NGAR-CHEUNG LAU

NOAA/Geophysical Fluid Dynamics Laboratory, Princeton University, Princeton, New Jersey

(Manuscript received 26 March 2004, in final form 30 November 2004)

ABSTRACT

The impact of the El Niño–Southern Oscillation (ENSO) on the atmospheric intraseasonal variability in the North Pacific is assessed, with emphasis on how ENSO modulates midlatitude circulation anomalies associated with the Madden–Julian oscillation (MJO) in the Tropics and the westward-traveling patterns (WTP) in high latitudes. The database for this study consists of the output of a general circulation model (GCM) experiment subjected to temporally varying sea surface temperature (SST) forcing in the tropical Pacific, and observational reanalysis products.

Diagnosis of the GCM experiment indicates a key region in the North Pacific over which the year-to-year variation of intraseasonal activity is sensitive to the SST conditions in the Tropics. In both the simulated and observed atmospheres, the development phase of the dominant circulation anomaly in this region is characterized by incoming wave activity from northeast Asia and the subtropical western Pacific. Southeastward dispersion from the North Pacific to North America can be found in later phases of the life cycle of the anomaly. The spatial pattern of this recurrent extratropical anomaly contains regional features that are similar to those appearing in composite charts for prominent episodes of the MJO and the WTP.

Both the GCM and reanalysis data indicate that the amplitude of intraseasonal variability near the key region, as well as incoming wave activity in the western Pacific and dispersion to the western United States, are enhanced in cold ENSO events as compared to warm events. Similar modulations of the MJO-related circulation patterns in the extratropics by ENSO forcing are discernible in the model simulation. It is inferred from these findings that ENSO can influence the North Pacific intraseasonal activity through its effects on the evolution of convective anomalies in the tropical western Pacific. On the other hand, there is little modification by ENSO of the circulation features associated with the WTP.

The combined effect of the MJO and WTP on the intraseasonal circulation in the North Pacific is studied. Based on multiple regression analysis, it is found that the MJO and WTP make comparable contributions to the variability in the midlatitude North Pacific. These contributions may be treated as a linear combination of the anomalies attributed to the MJO and WTP separately.

1. Introduction

a. Modes of intraseasonal variability in the extratropics

The nature and dynamical origin of midlatitude atmospheric perturbations with time scales of 10 days to a season have long been of interest to the meteorological community. Particular attention has been devoted to several modes of variability on these time scales in the North Pacific sector, namely, teleconnection patterns with geographically fixed centers of action, westward-traveling patterns (WTP) in high latitudes, and the extratropical anomalies associated with the Madden–Julian oscillation (MJO) in low latitudes.

Many early studies have indicated that the low-frequency variability of the wintertime circulation in the extratropics tends to be organized about some preferred spatial patterns (e.g., Kutzbach 1970; Dickson and Namias 1976; Namias 1978; van Loon and Rogers 1978; see also the review section of Wallace and Gutzler

* Current affiliation: International Pacific Research Center, School of Ocean and Earth Science and Technology, University of Hawaii at Manoa, Honolulu, Hawaii.

Corresponding author address: Dr. Chi-Yung Tam, IPRC, SOEST, University of Hawaii at Manoa, 1680 East–West Road, POST Bldg., Honolulu, HI 96822.
E-mail: chiyung@hawaii.edu

1981). Wallace and Gutzler (1981) systematically documented a set of teleconnection patterns of the sea level pressure and 500-mb height fields. One of the most prominent patterns in this set is the Pacific–North America (PNA) pattern, which consists of a north–south seesaw in the North Pacific and centers of action in Canada and the southeastern United States. Dole (1986) showed that blocking flows in the North Pacific tend to acquire PNA-like features. Thus, the PNA pattern is a strong contributor to intraseasonal variability in that region.

In addition to teleconnection patterns with stationary nodes and antinodes, there are also intraseasonal phenomena with propagative characteristics. Branstator (1987) and Kushnir (1987) found retrograding planetary-scale flow patterns in high-latitude regions, with typical periods of about 3 weeks. They do not resemble any teleconnection patterns identified by Wallace and Gutzler (1981), and behave more like external Rossby waves. This interpretation is supported by an analysis of the vorticity budget related to the WTP (Lau and Nath 1999).

The MJO is a principal intraseasonal phenomenon in the Tropics (Madden and Julian 1971, 1972). The observational study of Knutson and Weickmann (1987) shows that the MJO is also linked to prominent extratropical circulation anomalies. Kiladis and Weickmann (1992) demonstrated that these oscillations are accompanied by large-scale wave trains spanning across the North Pacific basin to North America. Higgins and Mo (1997) found that persistent circulation events in the North Pacific are preceded by convection and large-scale divergent motion related to MJO activity in the tropical western Pacific.

b. *Impact of ENSO on North Pacific intraseasonal variability*

Namias (1986) noted that circulation anomalies over North America tend to have stronger month-to-month persistence during El Niño winters, suggesting that intraseasonal activity in the extratropics is sensitive to the phase of ENSO. Palmer (1988) found that the growth of rms errors of extended-range forecasts in the Pacific sector is closely related to the polarity of a PNA-like pattern. His barotropic model experiments indicate that a negative PNA-like pattern yields a more unstable background state and hence larger eddy growth rates. This result is noteworthy because the anomalous seasonal mean circulation during warm (cold) ENSO events resembles a positive (negative) PNA pattern (Horel and Wallace 1981). In other words, ENSO might influence intraseasonal activity in the extratropics through its effect on the stability of the basic state.

Renwick and Wallace (1996) presented firm evidence on the impact of ENSO on blocking frequencies. They showed that blocking episodes are less likely to occur during warm ENSO years than otherwise, and the strongest effect is found over the Bering Strait. They also reported that, during cold events, intraseasonal activity is enhanced over the eastern Siberian coast, Alaska, and northwestern Canada.

The ability of atmospheric general circulation models (GCMs) to reproduce the impact of ENSO on the North Pacific intraseasonal activity is also assessed in a number of studies. The modeling work of Mullen (1989) indicates that in La Niña–like situations, the total number of block days is increased over the Aleutians and decreased over the northwestern Canadian coast. Chen and Van den Dool (1997) showed that blocking frequencies are increased (decreased) over the North Pacific and North America during cold (warm) events. They argued that the simulated blocking flows there are more effectively forced and maintained by the more active high-frequency eddies during cold events. Compo et al. (2001), based on modeling experiments with large ensemble sizes, found that both the tropical precipitation and extratropical circulation on intraseasonal time scales are strongly affected by ENSO. They suggested that tropical forcing might be an important factor in determining variability in the extratropics.

c. *Issues to be addressed in this study*

In this paper, the impact of ENSO on the atmospheric intraseasonal variability in the extratropics is examined, with emphasis on the role of the MJO and WTP. A number of observational studies show that ENSO affects the propagation and preferred geographical location of MJO-related convective activity (Anyamba and Weare 1995; Fink and Speth 1997; Vincent et al. 1998; Hendon et al. 1999). In particular, warmer SST near the central Pacific seems to favor farther eastward penetration of the anomalous convection during El Niño events. On the other hand, convective signals are more confined to the far western Pacific during La Niña events. Such modulation of the MJO by ENSO might have an impact on the extratropical intraseasonal variability, in view of the ability of the MJO-related convection to excite Rossby wave trains in the North Pacific. Another important contributor to extratropical intraseasonal circulation is the WTP, the properties of which might also be affected by ENSO. The goal of this study is to delineate the relationship between MJO, WTP, and intraseasonal ciruclation in the extratropical North Pacific, and the influences of ENSO on these modes of variability. Specifically, the following questions will be addressed:

- How do the recurrent intraseasonal circulation anomalies in the North Pacific–North American sector evolve in space and time? What are the impacts of ENSO on these anomalies?
- How are the MJO and WTP related to these recurrent circulation features?
- How does ENSO, through its effect on the MJO and WTP, affect these anomalies?
- How do the extratropical anomalies associated with the MJO and WTP interact with each other?

Analyses in this paper make use of both observations and output from a GCM that is capable of producing a high level of MJO activity, as has been demonstrated in the diagnoses by Hendon (2000) of output from the same model. For the GCM simulation examined in this study, Tam (2003) showed that the zonal wind and large-scale divergent circulation have prominent wavenumber-1 signatures with a period of ~50 days. Moreover, the MJO-related convection in the model atmosphere is affected by ENSO in a way consistent with observations (see section 5).

This paper is organized as follows. In section 2, the GCM and the experimental setup, as well the observational dataset, are described. The wintertime intraseasonal variability of the extratropical circulation, and its modulation by ENSO are studied in section 3. Recurrent intraseasonal circulation features in the North Pacific sector are examined in section 4. The extratropical circulation anomalies related to the MJO and WTP, and the effects of ENSO on these anomalies, are described in section 5. The interaction between extratropical anomalies linked to the MJO and WTO is the subject of section 6. Discussions and summary are given in section 7.

2. Description of datasets

a. The GCM experiment

In this study, the output from a numerical experiment using the Geophysical Fluid Dynamics Laboratory (GFDL) climate GCM is analyzed. The GCM has a rhomboidal truncation at 30 wavenumbers, and has 14 unevenly spaced sigma levels. A smoothed realistic topography is incorporated in the lower boundary. Physical processes such as radiative transfer, ground hydrology, and gravity wave drag are included. The clouds in the model atmosphere are predicted, and convection is parameterized using the moist convective adjustment scheme of Manabe et al. (1965). Bulk aerodynamic formulas are used for surface wind stress, sensible heat flux, and evaporation. Gordon and Stern (1982) and Broccoli and Manabe (1992) gave more detailed descriptions of the model.

The GCM experiment is described by Lau and Nath (2003, see the description of their control experiment). This experiment was conducted with monthly varying sea surface temperature (SST) prescribed within the deep tropical eastern Pacific (DTEP; 15°N–15°S, 172°E to the South American coast) from 1950 to 1999. Outside of DTEP, climatological SST was imposed. In other words, interannual variation in the SST field outside of the DTEP is excluded. The experiment comprises eight 50-yr integrations, with each run being conducted using the same sequence of boundary forcing but different initial atmospheric conditions. Daily archived values are used in all analyses. Final results presented are based on ensemble averages over the eight individual integrations.

b. Observational data

The observational dataset for this study is based on the products from the National Centers for Environmental Prediction–National Center for Atmospheric Research (NCEP–NCAR) reanalysis project (Kalnay et al. 1996). In particular, it comprises the daily values of the upper-air winds, archived on a 2.5° × 2.5° latitude–longitude grid. For the purpose of examining the climatological behavior of intraseasonal acvtivity, reanalysis products within the period of 1979–99 are used. In studying ENSO-related variability, analyses are based on data from 1950 to 1999. For ease of comparison with GCM results, all reanalysis data are interpolated on the same grid as that of the GCM.

3. Intraseasonal activity and its interannual variations

To depict the level of intraseasonal activity at various geographical locations, the root-mean-squares (rms) of the 10–60-day filtered 300-mb height field (Z_{300}) in the November–March period is computed. Figures 1a,b show the result based on GCM (reanalysis) data for all years in the 1950–99 (1979–99) period. Here, and in the rest of the study, bandpass filtering is achieved by using a 141-weight Lanczos filter. The 10-day cutoff is chosen to exclude fluctuations related to synoptic-scale activity. The two charts indicate strong activity with comparable amplitudes over the North Pacific and the North Atlantic. The maxima in rms are located over the central and eastern part of the ocean basins, that is, in the jet exit regions. Strong activity extends eastward to northwestern North America and northern Eurasia.

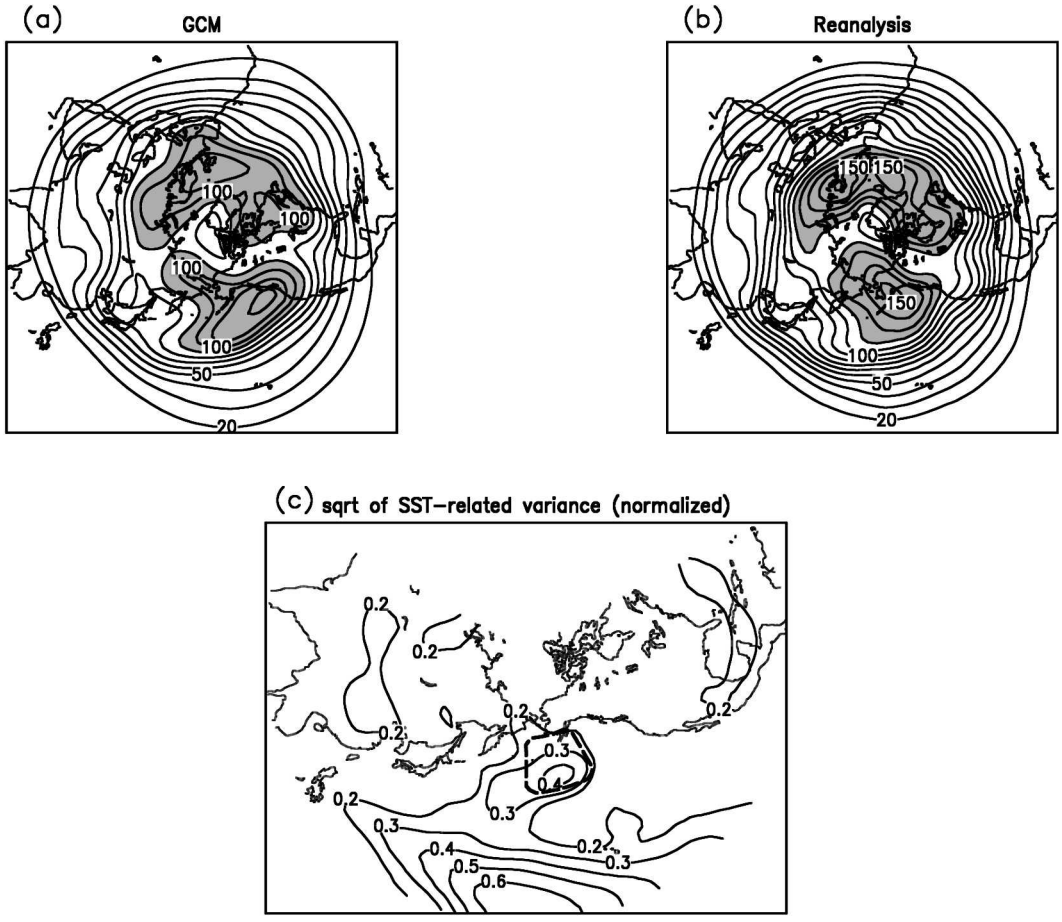

FIG. 1. (a), (b) The rms of the 10–60-day filtered 300-mb geopotential height for the Nov–Mar season, based on GCM and NCEP–NCAR reanalysis data, respectively. Contour interval is 10 m. Shading indicates values greater than 90 m (120 m) for GCM (reanalysis) patterns. (c) Square root of the ratio of SST-related variance of η to the total (SST-related plus internal) variance of η, based on GCM data. η is the rms of 10–60-day filtered 300-mb height computed for the Nov–Mar season in each year. Contour interval is 0.1. The border of the North Pacific key region is indicated by dashed lines.

It is noticed that rms amplitudes of the reanalysis pattern are about 20%–25% stronger than the simulated values. For the reanalyses, the most vigorous intraseasonal activity in the North Pacific sector is located over Alaska, whereas the strongest variability in the model atmosphere occurs near the northwestern North American seaboard. Overall, the strongest intraseasonal perturbations reside in higher latitudes in the observed atmosphere than in the model simulation.

Due to internal atmospheric variability and changes in the boundary forcing, it is well known that the level of intraseasonal activity fluctuates from year to year. Of particular interest to this study are the interannual variations of intraseasonal activity resulting from SST perturbations. The relative amplitude of such SST-related variations can be inferred from the GCM data. The rms of the 10–60-day filtered Z_{300} in the November–March period is calculated for *each year* and for each of the eight ensemble members. Its value is denoted by η. The "external variance" of this population of η values is obtained by first computing the eight-member mean $\{\eta\}$ for each year, and then evaluating the temporal variance of the time series of $\{\eta\}$ (see details in appendix A). By virtue of the design of the model experiment, this external variance can be attributed to the interannual variability of the imposed SST. The square root of a modified version of this external variance, expressed as a fraction of the "total variance" of η (see appendix A), is displayed in Fig. 1c. The pattern in this figure indicates that the interannual variation of intraseasonal activity related to the SST conditions is large over a broad region in the North Pacific, with a local maximum to the south of the Aleutians. Within the region 40°–60°N, 180°–150°W (outlined by

dashed contours), the square root of the external variance is about 30%–40% of that of the total variance. This region will be referred to as the "key region." In the model atmosphere, the intraseasonal anomalies proximate to this site should be sensitive to the SST in the DTEP region, as will be demonstrated in the following sections. It is noteworthy that the spatial pattern in high latitudes in Fig. 1c is different from that of the rms of Z_{300} shown in Fig. 1a, in which the largest amplitude is found near the northwestern North American seaboard. The SST-related variability also has large values in the tropical central Pacific. This feature could be related to the impact of ENSO on tropical intraseasonal activity.

Following Renwick and Wallace (1996), the ratio of the composite of the square of η (i.e., variance of the filtered Z_{300}) over cold ENSO events to the corresponding composite over warm events is shown in Fig. 2, for GCM and reanalysis datasets. Nine warm episodes and nine cold episodes in the period of 1950–99 are selected. The warm ENSO events chosen are 1957/58, 1965/66, 1969/70, 1972/73, 1976/77, 1982/83, 1987/88, 1991/92, and 1997/98. The cold events are 1950/51, 1954/55, 1955/56, 1964/65, 1970/71, 1973/74, 1975/76, 1988/89, and 1998/99. Activity over many parts in the subtropical and high-latitude Pacific is enhanced during cold events as compared to warm events. In the GCM simulation, the strongest enhancement is located over the Aleutian Islands. Suppressed activity over the midlatitude eastern North Pacific is discernible in the cold phase. Not surprisingly, regions with a strong impact of ENSO broadly correspond to the locations where the external variance of η is large (see Fig. 1c).

The GCM results agree reasonably well with those based on reanalysis data. Discrepancies are seen over east Asia, as well as near the Bering Strait where the activity enhancement in cold events occurs in relatively higher latitudes in the reanalysis pattern. Overall, the results in the North Pacific sector of Fig. 2 are in accord with those of Renwick and Wallace (1996) and Compo et al. (2001).

The impact of ENSO on the intraseasonal variability is also assessed by comparing the occurrence frequencies of persistent circulation episodes in different phases of ENSO. To define a persistent episode, daily values of Z_{300} averaged over the region of 40°–65°N, 170°E–150°W are first obtained.[1] The rms (σ) of the area-averaged Z_{300} time series is then computed using 10–60-day filtered data from November to March for all years. A persistent anomalous episode is identified

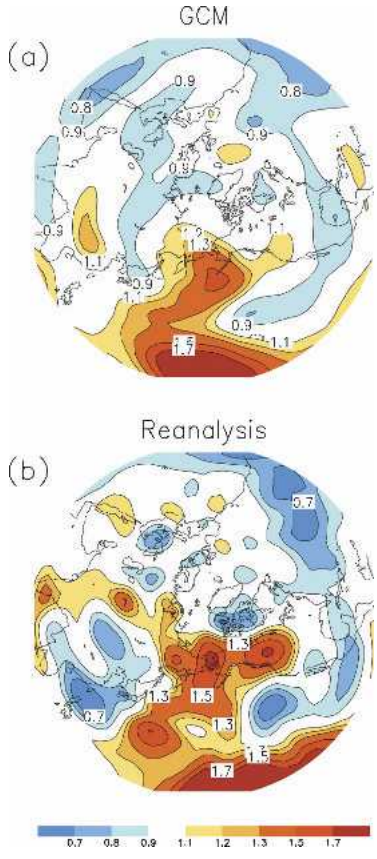

FIG. 2. Ratio of the cold-to-warm ENSO composite of the variance of 10–60-day filtered 300-mb geopotential height, for the Nov–Mar period. Result is based on (a) GCM and (b) NCEP–NCAR reanalysis data. Contour interval is 0.1. Contours for 1.0 are omitted. For the GCM pattern, ratios greater than 1.1 or less than 0.9 exceed the 95% significance level. The corresponding threshold values for reanalysis results are 1.3 and 0.7.

whenever the absolute value of the 10–60-day fluctuations in this local area mean of Z_{300} is greater than 0.5 σ for at least 10 consecutive days. This method is very similar to the one used by Dole and Gordon (1983) and Lau and Nath (1996). The frequencies of occurrence of these "0.5 σ episodes" during warm and cold ENSO events are shown in Fig. 3, based on GCM and reanalysis data. Results from both datasets indicate that persistent episodes are more frequent during cold events. The same computation is repeated using GCM data to obtain the frequencies of events that exceed the higher thresholds of 0.75 and 1 σ. Again, persistent events are more likely to occur in the cold phase than in the warm phase, indicating that inferences on ENSO modulation of prolonged episodes are not sensitive to the choice of the threshold magnitude. The statistics of blocking events given by Renwick and Wallace (1996) exhibit a similar dependence on the ENSO polarity.

[1] This domain encompasses the previously defined key region.

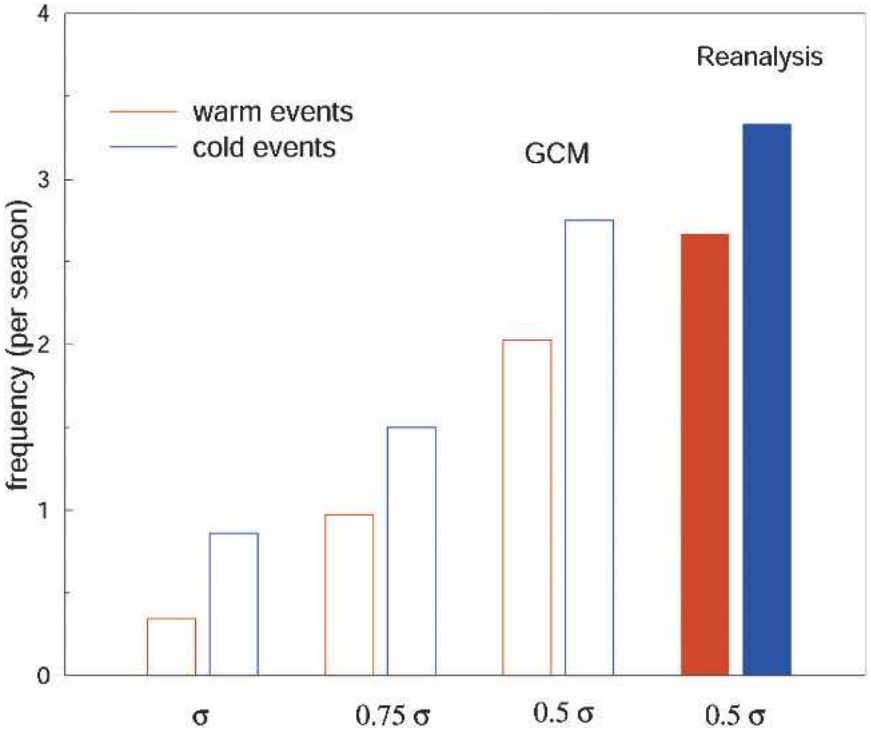

FIG. 3. Frequency of occurrence for persistent circulation episodes with amplitudes exceeding 0.5 σ for reanalysis (filled columns), and for GCM (first set of open columns from the right), during warm (red columns) and cold (blue columns) ENSO events. Also shown are frequencies of model-simulated episodes with amplitudes exceeding 0.75 and 1 σ.

4. Recurrent circulation anomalies over the North Pacific

a. Climatological characteristics

As discussed in the previous section, properties of the circulation anomalies proximate to the key region are particularly sensitive to the imposed SST in the model experiment. Before studying the influence of ENSO on these anomalies, their climatological characteristics are first examined using data for all years. To depict the typical evolution of these perturbations, meteorological fields are regressed at various temporal lags upon a (normalized) "reference time series" comprising the daily values of the 10–60-day filtered Z_{300} averaged over the key region. This regression method is applied to data of the 300-mb height from November to March for all years in the 1950–99 (1979–99) period for the GCM (reanalyses), and results for the two datasets are shown in Fig. 4. Three stages of evolution are identified for the life cycle of these typical circulation anomalies. They are depicted by averages of the regression charts for the lags of −5 to −2, −1 to +1, and +2 to +5 days, and will be referred to as the developing, mature and decay stages, respectively. Results based on the model and reanalysis datasets agree reasonably well, except that anomalies in the reanalysis patterns are relatively stronger in high-latitude regions and over North America. The following description applies to both model and reanalysis results. We shall henceforth refer to the disturbances in Fig. 4 as the "recurrent" intraseasonal anomalies in the North Pacific–North American sector.

In the developing stage (Figs. 4a,b), a ridge over the North Pacific is amplifying rapidly. Negative height anomalies are seen to the south and east of this ridge. Together these anomalies form a wave train extending from the subtropical North Pacific to North America. There is another negative anomaly east of Siberia, which is part of an east–west-oriented string of perturbations in the 50°–70°N zone. In the mature stage (Figs. 4c,d) the ridge in the North Pacific attains its maximum strength. The anomalous trough to its southeast has amplified substantially over northwestern United States, and a positive anomaly emerges over the southeastern Unites States. This southeastward development downstream of the key region is suggestive of the occurrence of Rossby wave dispersion. The subtropical

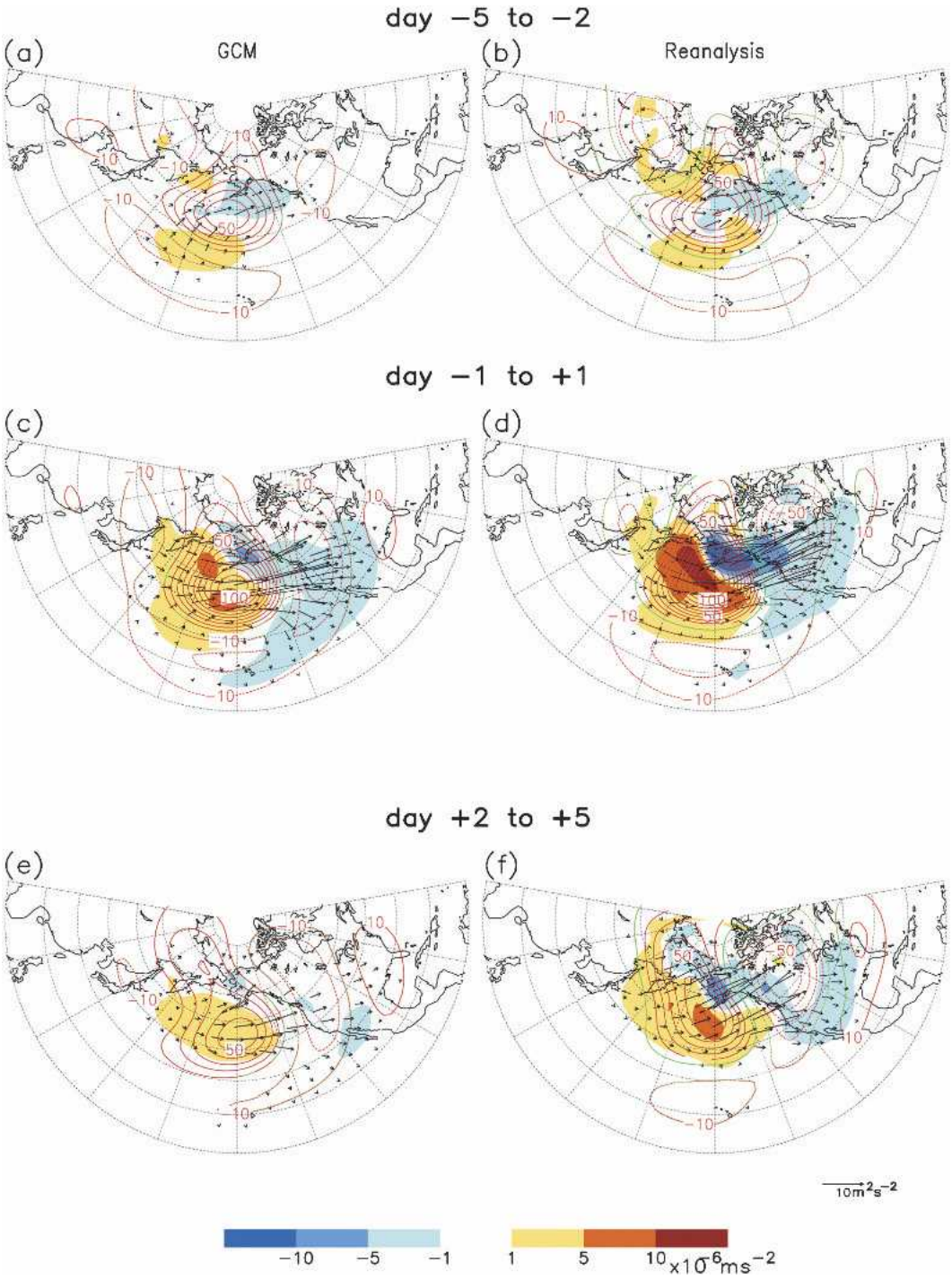

FIG. 4. Regression coefficients (contours) of 300-mb height perturbations at individual grid points upon the normalized time series of 10–60-day filtered 300-mb height averaged over the North Pacific key region (see Fig. 1c). Patterns are obtained by averaging regression maps over the lags of (a), (b) −5 to −2, (c), (d) −1 to 1, and (e), (f) 2 to 5 days. (left) For GCM data, height perturbations above (below) the 99% significance level are depicted by red (green) contours. (right) For reanalysis data, red (green) contours indicate significance above (below) the 95% level. Contour interval is 10 m. Zero contours are omitted. The wave activity vectors (arrows) and their divergence (shading) are superposed on the regression charts. Vectors are displayed only at locations where the absolute magnitude of their divergence is greater than 0.5×10^{-6} m s^{-2}. GCM (reanalysis) results are based on all years in the 1950–99 (1979–99) period.

low anomaly shifts eastward toward the eastern Pacific. The principal anomalies in the North Pacific–North American sector almost coincide with the centers of action of the PNA pattern (Wallace and Gutzler 1981). The anomaly over the northeastern Asian coast is seen to migrate southward. In the decay stage (Figs. 4e,f), most of the anomalies are weaker, but the wave train over North America is still discernible. The center of the North Pacific ridge remains quasi-stationary throughout the life cycle. However, the northern portion of this ridge (in the 60°–80°N zone) is seen to migrate westward with time. Such retrogression is reminiscent of the typical evolution of the circulation features associated with the WTP (see section 5).

Also shown in Fig. 4 are wave activity vectors of Takaya and Nakamura (2001) and their horizontal divergence (shading). The horizontal components of the activity vector **W** are given by[2]

$$(W_x, W_y) = \frac{1}{2|\mathbf{U}|}[U(\psi_x^2 - \psi\psi_{xx}) + V(\psi_x\psi_y - \psi\psi_{xy}), U(\psi_x\psi_y - \psi\psi_{xy}) + V(\psi_y^2 - \psi\psi_{yy})],$$

where ψ is the perturbation streamfunction and the subscripts on the rhs represent partial derivatives. Here $\mathbf{U} = (U, V)$ is the two-dimensional time mean flow. Convergence of the activity flux can lead to amplification of the wave pseudomomentum M, which is equal to a combination of the energy and enstrophy of eddies (see Takaya and Nakamura 2001). Wave activity vectors are computed based on regression maps of Z_{300}. Since the expression of **W** is phase independent, these vectors are useful in providing snapshots of wave dispersion in each stage of the evolution of the recurrent circulation anomalies.

In the developing stage, there is incoming wave activity from the subtropical Pacific and northeast Asia. Convergence of the activity flux occurs over the Gulf of Alaska. In the mature stage, activity flux convergence seems to accompany the development of anomalies in North America. Activity vectors in high latitudes are mostly zonally oriented, indicating eastward dispersion in that region. Another noteworthy feature in the southeastern portion of the North Pacific ridge is the southward turning of wave activity vectors toward the subtropical eastern Pacific. In the decay stage, some divergence of activity flux from the ridge is still discernible, and eastward dispersion now prevails over the North Pacific.

b. The impact of ENSO

To study the impact of ENSO on the behavior of the intraseasonal anomalies, the same regression method is applied separately to data for warm and cold ENSO events. Figures 5 and 6 show the results based on the GCM and reanalysis dataset, respectively. The GCM patterns are discussed first. Anomalies in the North Pacific–North American region are comparatively stronger throughout their life cycle during cold events. This is consistent with the cold-to-warm variance ratio shown in Fig. 2. In the developing stage (Figs. 5a,b), there is more incoming wave activity from the subtropics in the cold ENSO phase. The cyclonic anomaly in the subtropical ocean is also stronger in this phase. During cold ENSO events, the activity flux directed to the North Pacific ridge center is more intense, and the development east of the ridge is more evident in this developing stage.

In the mature stage (Figs. 5c,d), there is still a substantial amount of incoming activity from the subtropics during cold events. Prominent southeastward Rossby wave dispersion occurs over the United States in cold events. The dispersion during warm events proceeds along two pathways (see arrows in Fig. 5c), with one branch being directed to northwestern North America, and another branch to the subtropical eastern Pacific. In the decay stage (Figs. 5e,f), anomalies over the northwestern North American seaboard are relatively stronger during cold events.

The GCM results (Fig. 5) agree with the reanalysis patterns (Fig. 6) in several respects. Observed perturbations are stronger throughout their life cycle during cold events as compared to warm events. In the developing stage (Figs. 6a,b), the subtropical Pacific anomaly is stronger in the cold ENSO phase. More convergence of activity flux into the North Pacific ridge and stronger dispersion downstream of the ridge occur during cold events. The reanalysis patterns for the mature and decay stages (Figs. 6c–f) further indicate that the wave train pattern over North America is modulated by ENSO: the positive anomaly is centered over southeast United States during cold ENSO episodes, while during warm episodes the wave train has a more zonal orientation, with the positive anomaly being located over the northeastern coast of North America.

In summary, it is found that ENSO affects the magnitude, circulation features, and dispersion characteris-

[2] This expression of **W** holds for quasi-stationary eddies only. There is also a vertical component of **W** not considered here. See Takaya and Nakamura (2001) for details.

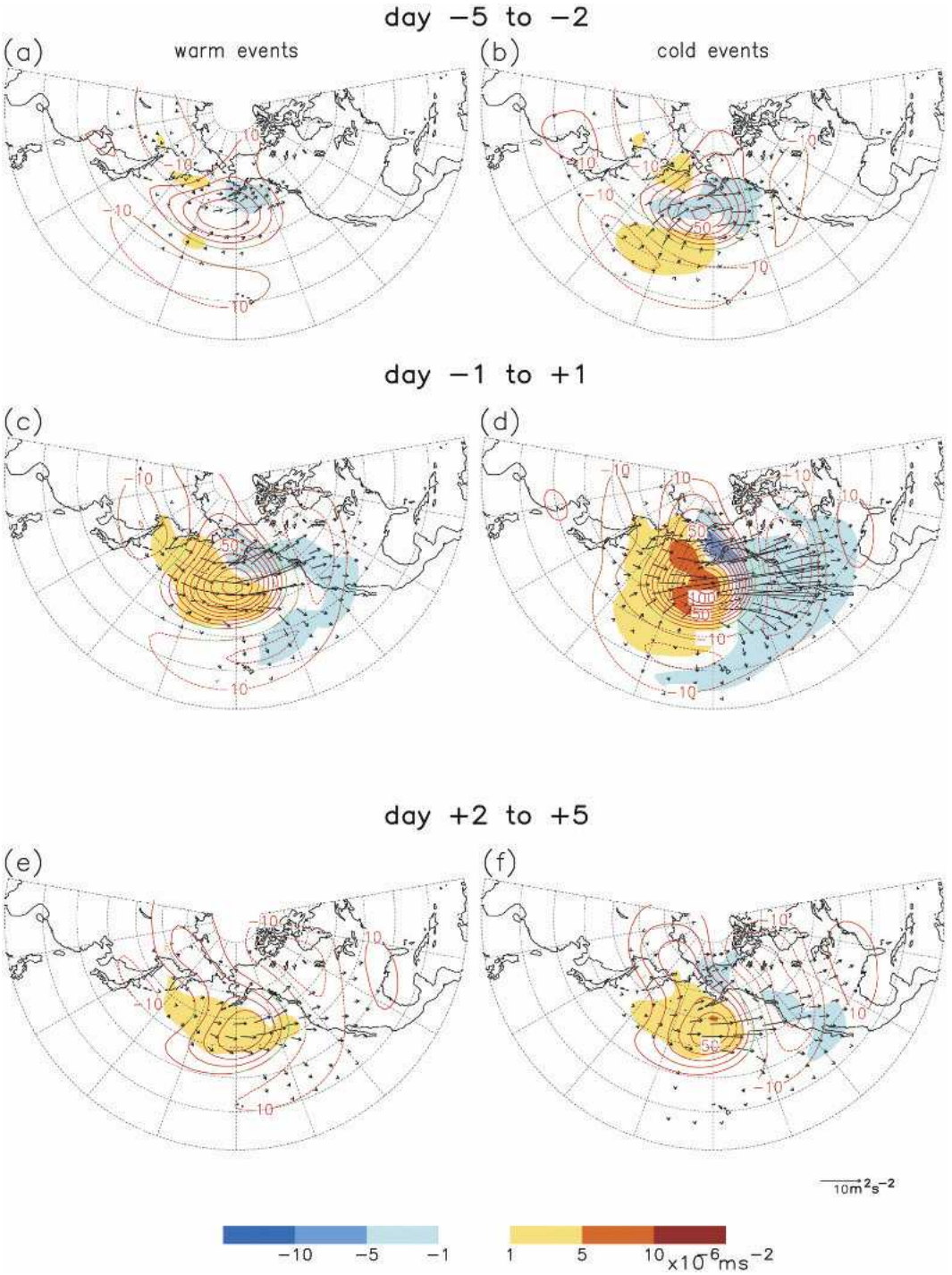

FIG. 5. Same as in Fig. 4, but for composites of GCM patterns over selected (a), (c), (e) warm and (b), (d), (f) cold ENSO events. Regression values above (below) the 95% significance level are indicated by red (green) contours.

tics of the intraseasonal anomalies over the North Pacific. There is stronger incoming wave activity from the subtropics during cold events. The subtropical anomaly over the western-central Pacific is stronger, and there are also stronger perturbations over the northwestern North American seaboard in the cold ENSO phase. For the GCM result, a Monte Carlo method is used to access the significance of the difference in the circulation

features in different phases of ENSO.[3] This test confirms that the aforementioned differences in the circulation features simulated in the warm and cold events are significant at the 95% level.

5. Extratropical circulation patterns associated with the MJO and WTP

a. Climatological characteristics

The MJO and WTP are strong contributors of intraseasonal variability in the North Pacific region (see section 1). In this section, extratropical circulation anomalies associated with these two modes are studied based on the GCM dataset. It will be shown that these anomalies are closely related to the recurrent circulation patterns identified in section 4.

To examine the evolution of the MJO- and WTP-related circulation anomalies, a composite method based on products of complex empirical orthogonal function (CEOF) analyses is used. For the MJO, the CEOF of the 10–100-day bandpass-filtered 200-mb velocity potential in the region of 20°N–20°S is computed. For the WTP, the CEOF of the Z_{300} field is computed based on 10–45-day bandpass-filtered data within 55°–90°N, 90°E–90°W (see appendix B). Using the time series of the temporal coefficients (i.e., the principal component, abbreviated as PC) of these leading CEOF modes, composite charts of meteorological fields in different phases of the MJO and WTP cycle are constructed as follows. An MJO or WTP episode is identified if the corresponding PC amplitude (i.e., the modulus of the complex PC coefficient) is greater than the threshold value of 0.75 standard deviation (sd) for at least 20 consecutive days, and the episode encompasses a total phase change of 2 π or more.[4] The MJO or WTP cycle is divided into eight bins according to their phases (i.e., the argument of the complex PC coefficient): 0 to $\pi/4$, $\pi/4$ to $\pi/2$, . . . , $7\pi/4$ to 2π, hereafter referred to as phase 1, 2, . . . , 8, respectively. The 10-day lowpass-filtered values of meteorological fields in various phases of all selected episodes are collected, and composite maps for individual phases are constructed by taking the average of these values in the corresponding phase bins.

Figure 7 shows the composites maps of Z_{300} in phase 7, 8, and 1 of the MJO and WTP cycles, [5] as computed using data for all years. For the MJO, a wave train originating from the subtropical western Pacific can be seen in phase 7 (Fig. 7a). Anomalies grow over the North Pacific, and there is southeastward development of perturbations over North America in phases 8 and 1 (see Figs. 7c,e). Throughout these phases the anomalous high over the central Northern Pacific remains stationary, while the center of the subtropical Pacific low is shifted eastward. The anomalies shown in phase 8 of the MJO broadly resemble the PNA pattern.

The composite chart for phase 7 of the WTP (Fig. 7b) is characterized by a wavelike pattern with a ridge over Alaska and troughs to its east and west. As inferred from the charts for phases 8 and 1 (Figs. 7d,f), the anomalous ridge gains strength as it travels westward over the Asia–America land bridge. The negative anomalies over eastern Siberia migrate southward. Anomalies related to the WTP are generally stronger in high latitudes. However, a midlatitude trough with moderate strength is also evident in the central and eastern Pacific. The evolution of the WTP in Figs. 7b,d,f bears some resemblance to that described by Branstator (1987), Kushnir (1987), and Lau and Nath (1999).

It is noteworthy that the MJO- and WTP-related circulation features are similar to the recurrent intraseasonal anomalies examined in Fig. 4, in terms of both their spatial features and temporal evolution. Resemblance between Fig. 4 and the MJO-related pattern is particularly notable in the subtropical and midlatitude Pacific as well as over North America. Correspondence between Fig. 4 and perturbations associated with the WTP is most evident in high latitudes and in northeastern Asia. In other words, the prevalent intraseasonal anomalies project strongly on the characteristic patterns related to the MJO and WTP.[6] The combined effects of the MJO and WTP on the extratropical circulation are also examined using a composite technique (referred to as "MJO + WTP" composites in section 6). The result of this analysis (not shown) indicates that constructive interference between the anomalies associated with the MJO and WTP yields circulation patterns that are very similar to those displayed in Fig. 4. The nature of the interaction between the extratropical

[3] Two sets of regression charts are computed based on model data from nine distinct, randomly chosen years. The difference between these two sets constitutes one sample, and 100 000 such samples are used for establishing the significance levels.

[4] There are about 800 (700) WTP (MJO) episodes for all years for all model integrations. During either warm or cold ENSO events, ~150 (125) WTP (MJO) episodes are identified.

[5] Note that the phases of the MJO and WTP are labeled independently of the other.

[6] The evolution of regional features in Fig. 7 correspond well to those of the recurrent anomalies in Fig. 4, so that phases 7, 8, and 1 of the MJO and WTP can be approximately identified with the time lag of −5 to −2, −1 to 1, and +2 to +5 days in Fig. 4, respectively.

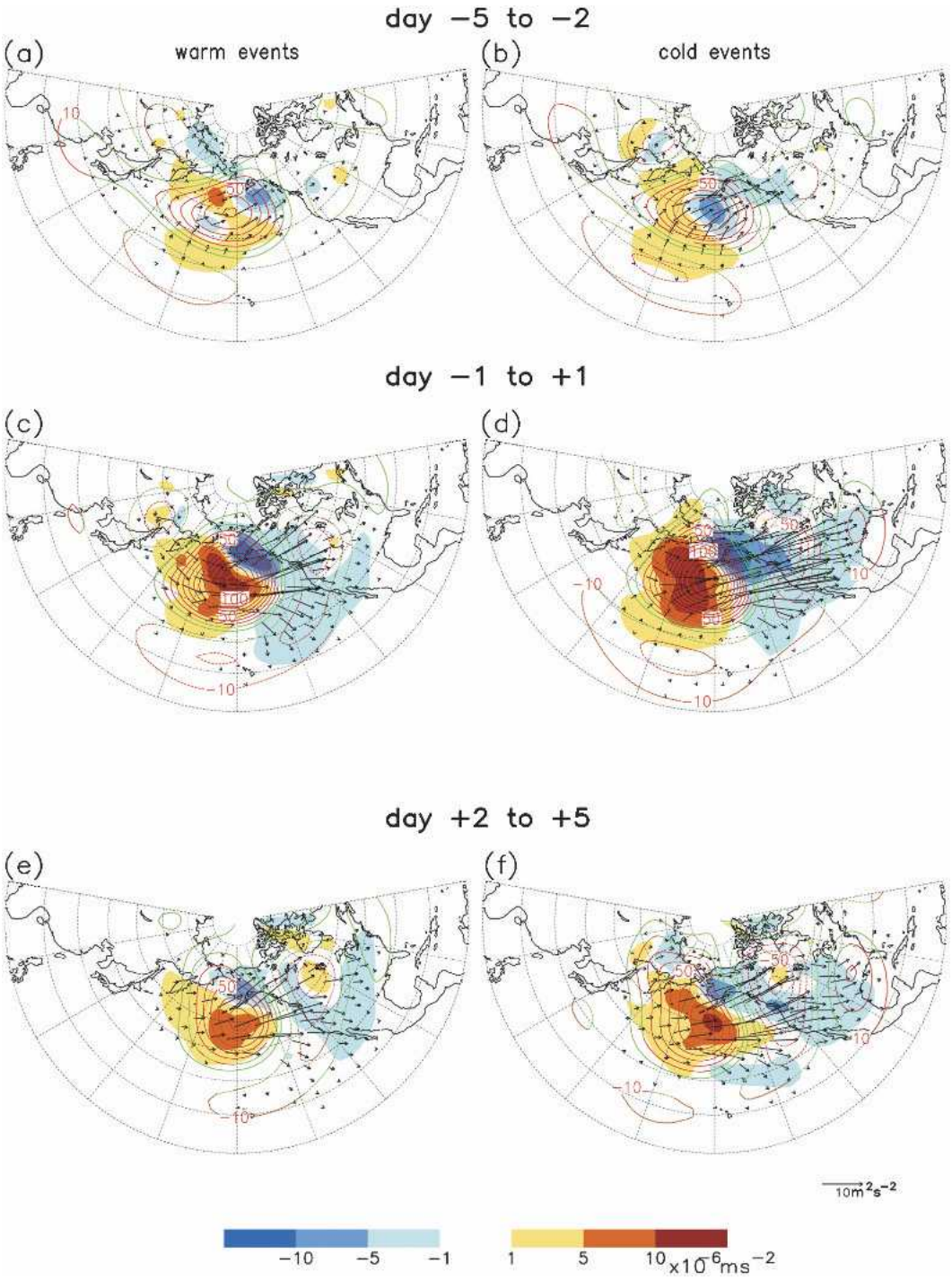

FIG. 6. Same as in Fig. 5, but for reanalysis data.

anomalies related to the MJO and WTP will be considered in section 6.

b. Modulation by ENSO

In section 4 it is shown that ENSO has an impact on both the amplitude and circulation features of the recurrent extratropical intraseasonal anomalies. It would be of interest to examine how ENSO affects these anomalies through its influences on the MJO and WTP. Figure 8 shows the Z_{300} and precipitation composites in different phases of the MJO during warm and cold ENSO events. In phase 7 (Figs. 8a,b), a wave train ex-

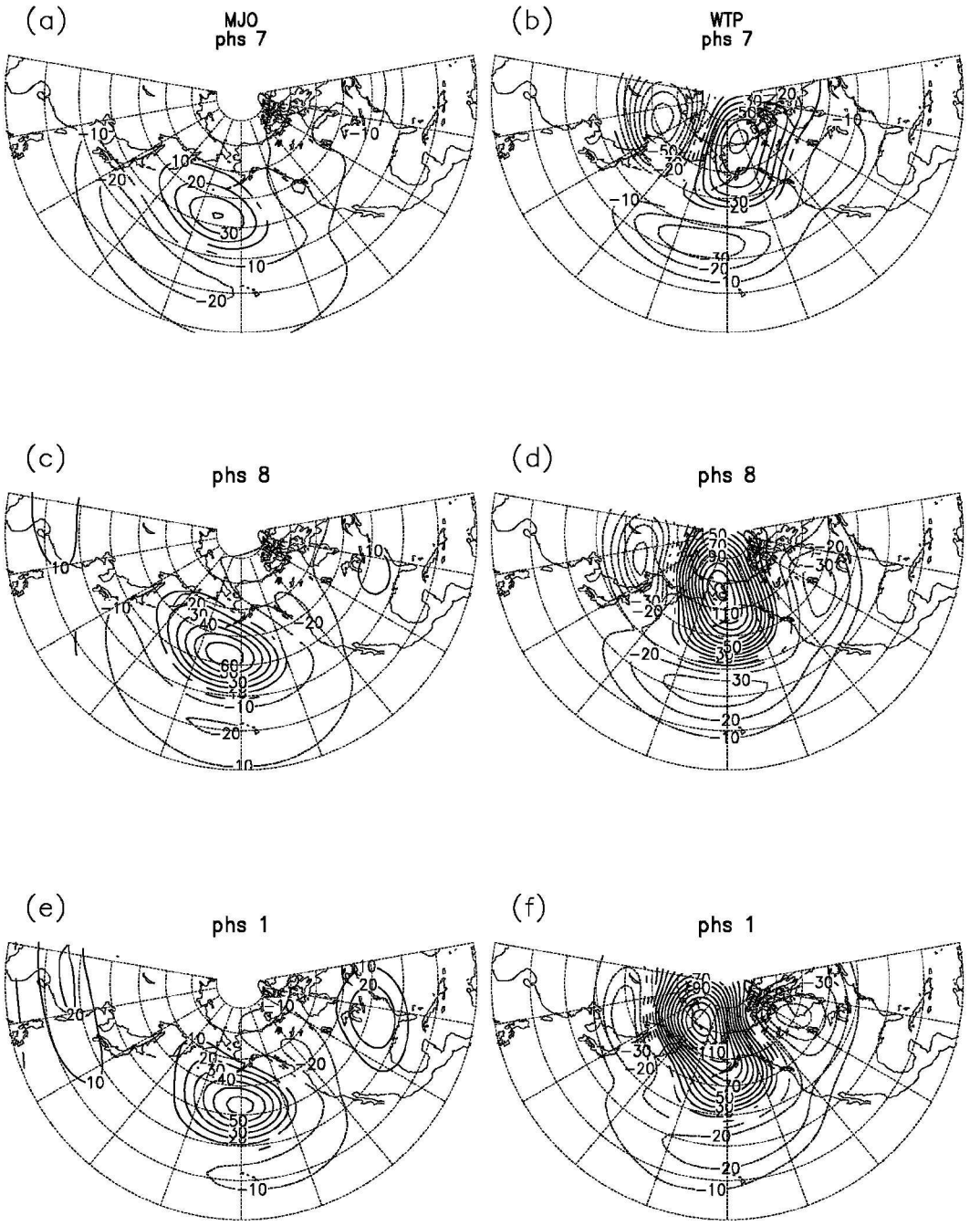

FIG. 7. Composite maps of GCM-simulated 300-mb height anomalies for selected phases of strong cycles of (a), (c), (e) MJO and (b), (d), (f) WTP. Results are based on all years in the 1950–99 period. Contour interval is 10 m. Zero contours are omitted. Contours are drawn only where anomalies exceed the 99% significance level.

tending from the subtropical Pacific to North America is discernible during both warm and cold events. However, in cold ENSO years the subtropical trough is more prominent in the western part of the Pacific Ocean and the North Pacific ridge is relatively stronger. The difference in the amplitude of the ridge in warm and cold phases of ENSO episodes might be related to the position of the ridge relative to the exit of the Pacific jet stream. Naoe et al. (1997) showed that Rossby waves tend to grow near jet exit regions. The displacement of

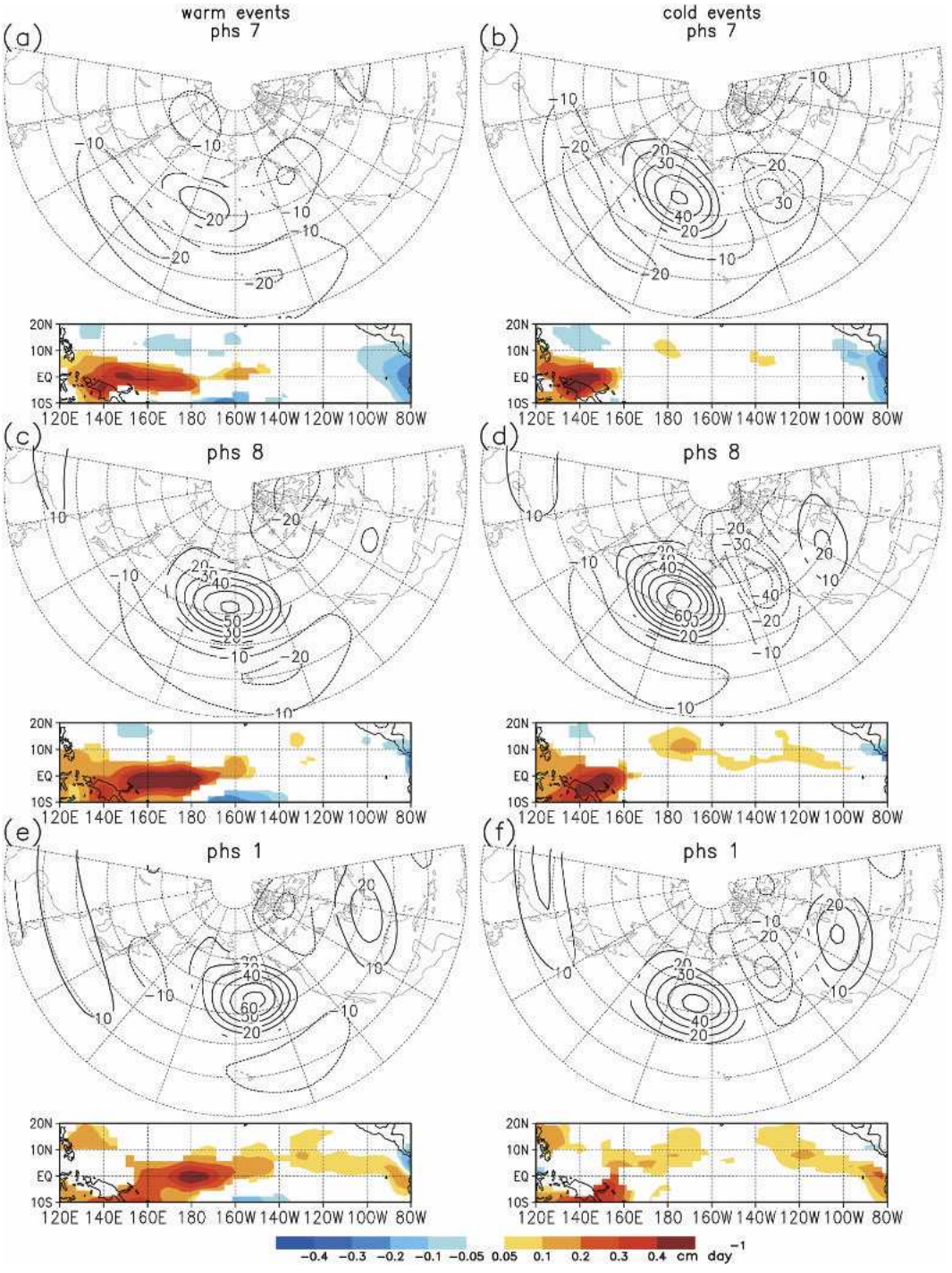

FIG. 8. Composite maps of GCM-simulated 300-mb height (contours; upper part of panels) and precipitation anomalies (shading; lower part of panels), for selected phases of strong MJO cycles occurring during (a), (c), (e) warm and (b), (d), (f) cold ENSO events. Contour interval is 10 m. Zero contours are omitted. All precipitation and height perturbations shown here exceed the 95% significance level.

the jet exit region eastward during warm events (not shown) could partially account for the weaker amplitude of the ridge in this phase of the MJO.

In phase 8, the anomalies in the subtropics, North Pacific, and North American seaboard remain almost stationary during cold events (Fig. 8d). There is also strong downstream development over North America in these events (see also phase 1, Fig. 8f). During warm

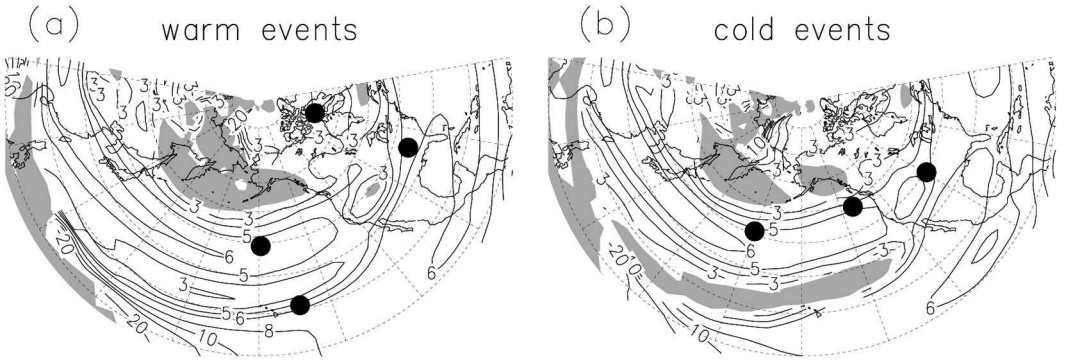

FIG. 9. Total wavenumber, K_s, based on composites of GCM data for the mean 300-mb zonal flow over (a) warm and (b) cold ENSO events. Contours correspond to values of 3, 4, 5, 6, 8, 10, 12, and 20. Shading indicates imaginary values. Black dots denote approximate locations of centers of action in phase 8 of the MJO (see Figs. 8c,d).

events (Fig. 8c), the center of the subtropical anomaly is located more to the east, and the trough downstream of the North Pacific ridge resides over northern Canada. Many of these effects of ENSO on the MJO-related perturbations are strikingly similar to those on the recurrent intraseasonal anomalies presented in section 4 (see Fig. 5).

Based on the three MJO phases depicted in Fig. 8, it can be seen that ENSO also has a strong impact on the evolution of tropical convection (see lower portions of each panel). MJO-related precipitation is more confined to the far western Pacific during cold events, and extends farther east to the date line during warm events. This displacement of convective activity in the model atmosphere is due to the SST conditions over the tropical Pacific in different phases of ENSO (Tam and Lau 2005). The resulting different MJO convection could account for part of the sensitivity of the wave train in Fig. 8 to the ENSO polarity, such as the stronger subtropical circulation features and the more stationary wave pattern during cold events as compared to warm events.

Besides the behavior of the tropical forcing, the extratropical mean state is also important in determining the MJO-related circulation. To relate the different dispersion characteristics to the mean flow structure in different phases of ENSO, the total wavenumber K_s during warm and cold events are plotted in Fig. 9. Here K_s is given by $\sqrt{(\beta - U_{yy})/U}$, where β is the meridional gradient of the Coriolis parameter, U is the mean 300-mb zonal wind in the November–March period, and subscripts denote partial derivatives. Hoskins and Ambrizzi (1993) showed that Rossby waves are refracted toward regions of larger K_s. Jet streams produce local maxima of K_s in their vicinity and can therefore serve as waveguides. During cold events in the eastern Pacific, K_s decreases rapidly southward on the subtropical side of the jet; whereas the rate of decrease of K_s in the same region is smaller during warm events. The difference in the pattern of K_s can be further related to the change of U during ENSO. During warm events, the zonal wind is increased over the subtropical central-eastern Pacific. The value of $-U_{yy}$ is also larger at about 25°N (not shown), leading to larger K_s there. On the other hand, the weaker jet in the same region leads to smaller values of K_s during cold events. These patterns of K_s imply less refraction or less effective trapping of Rossby waves over that part of the eastern Pacific in the warm ENSO phase, thus facilitating a more distinct equatorward branch of wave dispersion toward the subtropical eastern Pacific during warm events. In contrast, most of the dispersion is channeled toward North America during cold events (see Fig. 5). The effects of the waveguide properties of the Pacific jet stream during warm and cold ENSO episodes on the extratropical anomalies associated with the MJO are illustrated by the locations of centers of action in phase 8 of the MJO cycle (black dots in Fig. 9). During warm events, a strong center is found over the subtropical eastern Pacific, suggesting southeastward dispersion from the North Pacific principal anomaly. On the other hand, the strong centers of perturbations are seen to be lying in almost the same latitude circle during cold events, indicating that wave dispersion is more zonal over the North Pacific–North American sector in the cold ENSO phase.

The impact of ENSO on the WTP is now examined. Composite charts of Z_{300} in phase 8 of the WTP during warm and cold events are shown in Fig. 10. Perturbations in high latitudes are stronger during cold events as compared to warm events. However, the spatial features of the circulation associated with the WTP during warm and cold ENSO episodes are rather similar. For other phases of the WTP (not shown), circulation

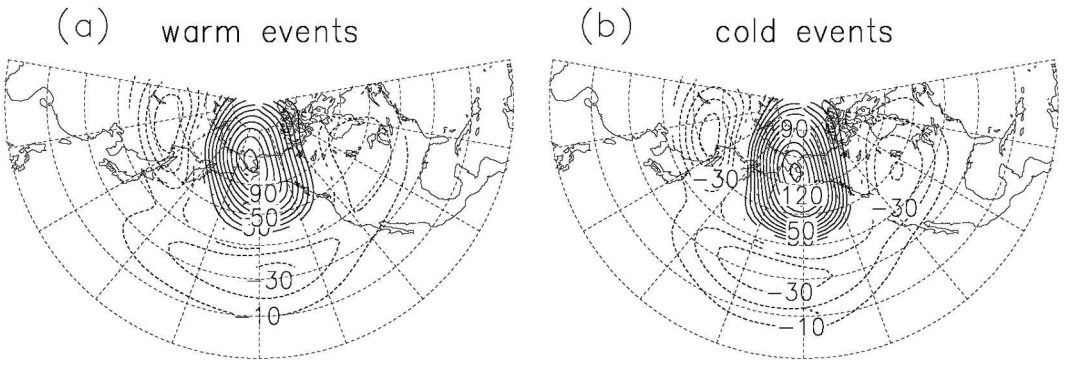

FIG. 10. Composite maps of GCM-simulated 300-mb height anomalies in phase 8 of strong WTP cycles occurring in (a) warm and (b) cold events. Contour interval is 10 m. Zero contours are omitted.

anomalies in warm and cold years also resemble each other. Hence the spatial patterns associated with the WTP exhibit a much weaker dependence on the ENSO phase as compared with the MJO-related anomalies.

In comparing the results in this subsection with those in section 4b, it is evident that the influences of ENSO on the extratropical signals associated with the MJO (Fig. 8) are similar to the ENSO modulation of the recurrent circulation patterns near the key region (Fig. 5); whereas the alteration of the WTP during warm and cold events (Fig. 10) are much less discernible in Fig. 5. Inspection of the tropical precipitation changes (not shown) accompanying the recurrent midlatitude anomalies in Fig. 4 reveals strong variations in convective activity over the tropical western Pacific. This relationship, together with the resemblance between Figs. 5 and 8, suggest that ENSO influences intraseasonal variability in the North Pacific mostly through its impact on MJO-related rainfall in the Tropics. To further illustrate the covariability of ENSO, MJO, and the extratropical circulation, the evolution of the precipitation and 200-mb velocity potential signals associated with the recurrent midlatitude circulation changes is shown in Fig. 11 separately for warm and cold ENSO events. These diagrams are constructed using lag regression upon the reference time series of 300-mb height over the key region (see section 4), and the regression values are averaged over the 10°N–10°S zone. During warm events the convection and velocity potential are seen to extend more eastward as compared to those during cold events. The differences in the location of convective heating during warm and cold ENSO episodes could excite different wave train patterns in the extratropics. For instance, the subtropical trough anomaly is more evident over the western part of the Pacific in cold events than in warm events (see Fig. 5), partly due to the stronger confinement of the precipitation forcing in that sector during cold episodes (Fig. 11). The strong resemblance between the tropical precipitation anomalies accompanying circulation changes over the North Pacific (Fig. 11) and those related to the MJO life cycle (Fig. 8) confirms the important role of the MJO in modulating intraseasonal variability in the extratropics during ENSO events.

6. Interaction between midlatitude anomalies associated with MJO and WTP

In the previous sections it is shown that certain regional signals of the recurrent intraseasonal anomalies in the North Pacific resemble those of the extratropical circulation changes related to the MJO and WTP. Based on the GCM dataset, the relative contributions of the MJO and WTP to intraseasonal variability over the North Pacific region will be quantified. Consider the following equation for the 10–60-day filtered Z_{300} field:

$$\hat{Z}_{300} = \Phi_{a_r} a_r + \Phi_{a_i} a_i + \Phi_{b_r} b_r + \Phi_{b_i} b_i. \qquad (1)$$

Here $\hat{Z}_{300}$ is expressed as a linear combination of four time series, two of them are related to the WTP and the other two to the MJO. The time series a_r *and* a_i are the standardized real and imaginary parts, respectively, of the PC for the leading CEOF of Z_{300}, which are used to characterize the WTP cycle (see section 5). Similarly, b_r and b_i are the real and imaginary parts of the leading PC for the 200-mb velocity potential field, and have been used to obtain the phase information of the MJO. It is noteworthy that the correlation between any two of the four time series is very small. In other words, each of them is practically independent of the others. The spatially dependent coefficients Φ can be computed using multiple regression. Their patterns are shown in Figs. 12a–d. Since a_i leads a_r by one-forth of a cycle (not shown), Φ_{a_r} and Φ_{a_i} (Figs. 12a,b) together depict retro-

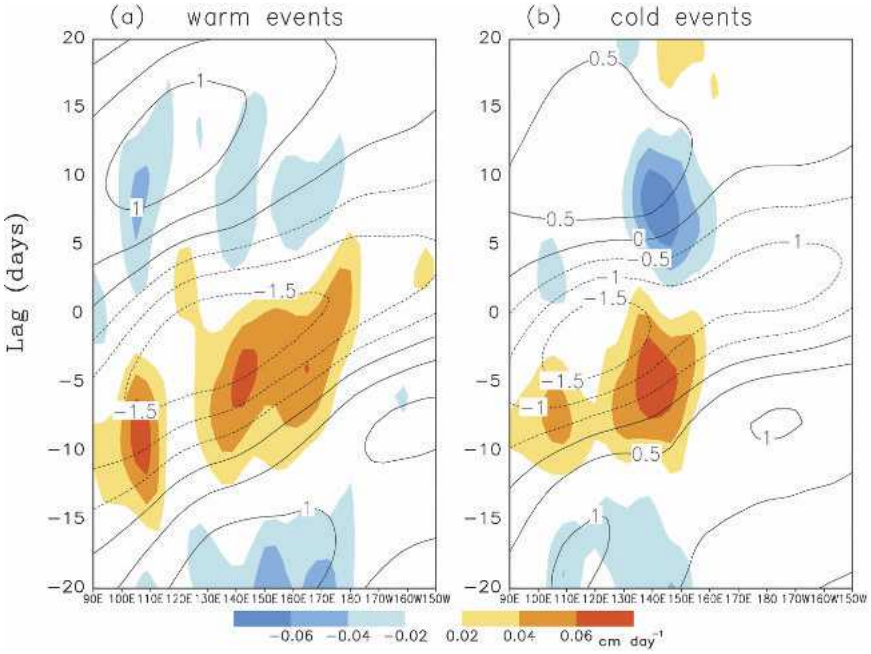

FIG. 11. Longitude–time distributions of lag regression coefficients of precipitation (shading) and 200-mb velocity potential (contours; interval: 0.5×10^6 m^2 s^{-1}) upon the normalized reference time series of 300-mb height in the North Pacific key region (see Fig. 1c), based on GCM data for the (a) warm and (b) cold ENSO years. Results are averaged over the 10°N–10°S zone.

grading Z_{300} perturbations in the high-latitude zone, with space–time characteristics similar to WTP composites shown in Figs. 7b,d,f. By the same token, Φ_{b_r} and Φ_{b_i} (Figs. 12c,d) together indicate a wave train originating from the subtropical Pacific, with perturbations developing over the North Pacific and North America. These patterns agree with the evolution of the MJO-related height anomalies as displayed in Figs. 7a,c,e.

The amplitude of the Z_{300} fluctuations due to the WTP can be obtained by computing the rms of $\hat{Z}_{300}$ with $\Phi_{b_r} b_r$ and $\Phi_{b_i} b_i$ being set to zero in Eq. (1). Analogously, the amplitude due to MJO activity is evaluated as the rms of $\hat{Z}_{300}$ with the deletion of $\Phi_{a_r} a_r$ and $\Phi_{a_i} a_i$ terms. Both of these amplitude measures are divided by the rms of the 10–60-day filtered Z_{300}, so as to express the WTP- and MJO-related variability as a fraction of the total amplitude. The amplitude ratios thus obtained are mapped in Figs. 12e,f for WTP and MJO components. As expected, the WTP component (Fig. 12e) is more prominent in high latitudes, with a secondary maximum in the amplitude ratio appearing over the central Pacific at about 30°N. The corresponding pattern for the MJO component is characterized by a broad maximum over the subtropical western and central Pacific, and another more localized maximum centered near 40°N, 160°W. Within the 40°–50°N zone over the North Pacific, the MJO and WTP component are comparable. This implies that the two phenomena make equally important contributions to the intraseasonal activity in that region.

In view of the comparable impact of the MJO and WTP on midlatitude intraseasonal variability, we proceed to study the nature of the interactions between extratropical circulation anomalies associated with these two individual components. We first define the composite height anomalies for phase category θ_χ of the MJO cycle and with threshold value of the PC amplitude s_χ (see section 5) as $\Phi(\theta_\chi, s_\chi)$. Here the subscript χ in θ and s signifies that these phase and amplitude measures are based on the leading CEOF of the velocity potential field χ_{200}. Analogously, the composite for the phase θ_Z of the WTP cycle with the amplitude threshold s_Z are denoted by $\Phi(\theta_Z, s_Z)$, where the subscript Z indicates that these parameters are obtained from the CEOF of the Z_{300} field. For instance, the composite maps shown in Figs. 7a,c,e are constructed with $\theta_\chi = 7$, 8, and 1, and $s_\chi = 0.75$ sd. In general, larger values of s_χ imply that stronger MJO episodes are being selected, and stronger circulation features would appear in the composite charts.

We next consider composite maps over those time periods when both MJO and WTP episodes occur.

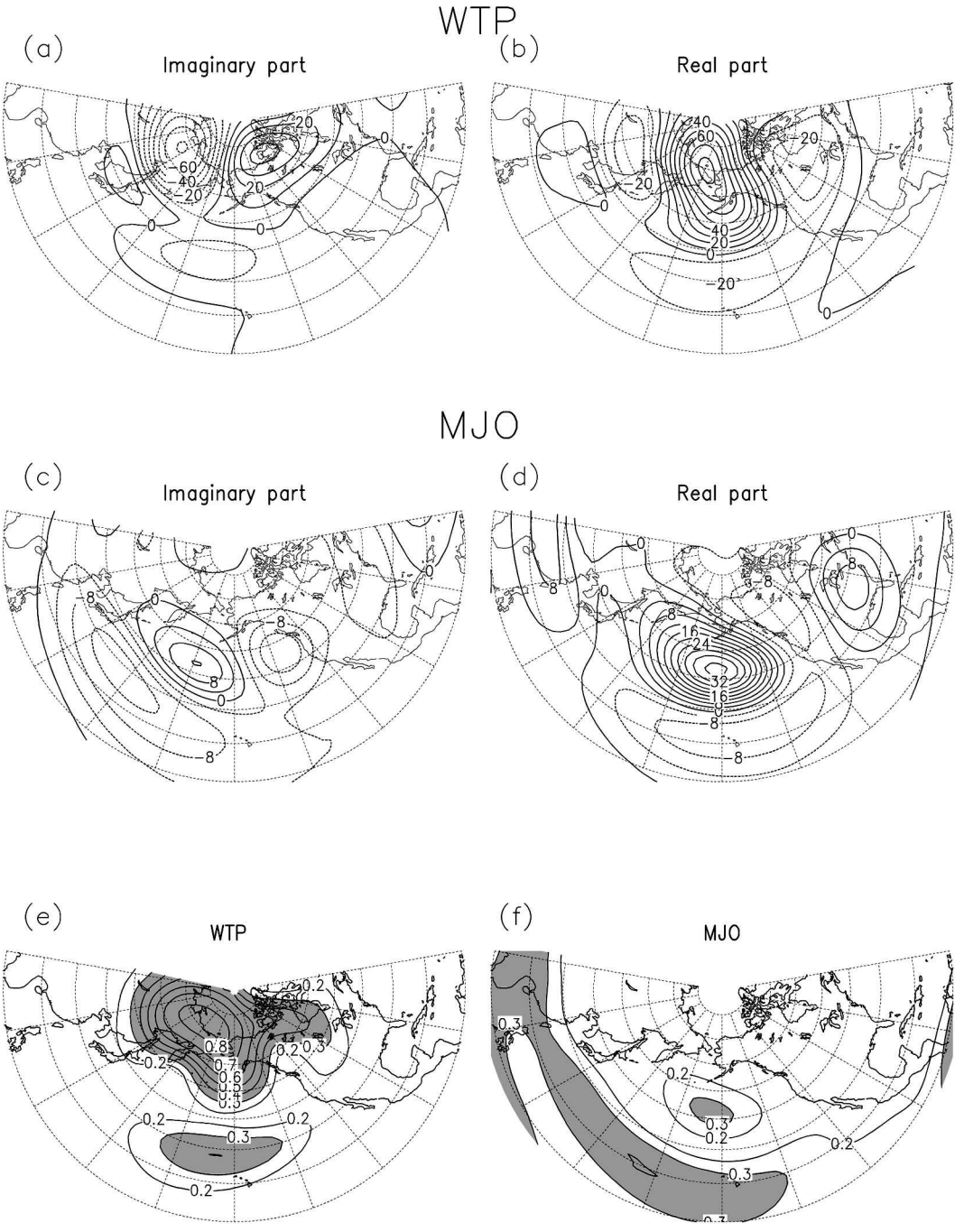

FIG. 12. Multiple regression coefficients of the 10–60-day filtered 300-mb height related to the (a) imaginary and (b) real parts of the PC for the first CEOF of Z_{300}, and to (c) imaginary and (d) real parts of the PC for first CEOF of the velocity potential χ_{200}. Contour intervals are (a), (b) 10 and (c), (d) 4 m. Ratios of the rms of 300-mb height associated with (e) WTP [i.e., first two terms on rhs of Eq.(1)] and (f) MJO [i.e., last two terms on rhs of Eq.(1)] to the total rms of the filtered height field. Contour interval is 0.1. Contours for 0.1 are omitted. All results are based on GCM data.

These patterns will hereafter be referred as "MJO + WTP composites," and are denoted by $\tilde{\Phi}(\theta\chi, s_\chi|\theta_Z, s_Z)$. Note that MJO + WTP composites can be constructed for each of the $8 \times 8 = 64$ possible combinations of the phases of the MJO and WTP. As expected, the MJO + WTP composite for $\theta_\chi = 8$, $\theta_Z = 8$, $s_\chi = s_Z = 0.75$ sd (not shown) contains a combination of the features appearing in the individual MJO [Fig. 7c, for $\Phi(\theta_\chi = 8, s_\chi$

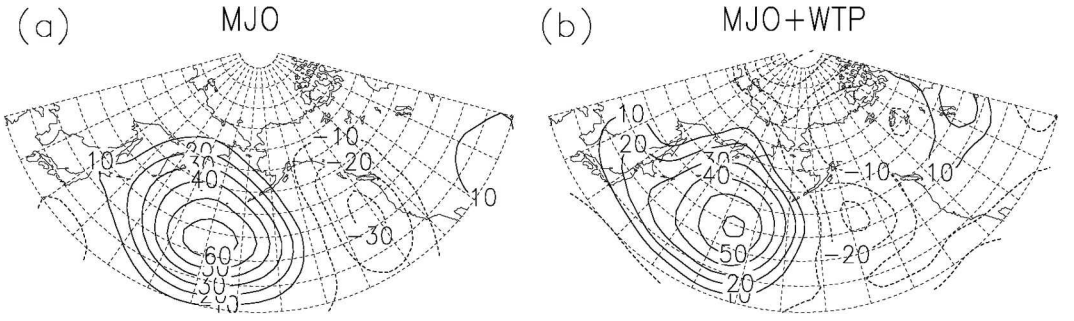

FIG. 13. Patterns of GCM-simulated 300-mb height anomalies for (a) $\delta\Phi(\theta_\chi = 8, s_\chi = 2.5$ sd) and (b) $\delta\tilde{\Phi}(\theta_\chi = 8, s_\chi = 2.5$ sd$|\theta_Z = 8)$. See text for details. Contour interval is 10 m. Zero contours are omitted.

$= 0.75$ sd)] and WTP [Fig. 7d, for $\Phi(\theta_Z = 8, s_Z = 0.75$ sd)] composites.

For the MJO cycle, we further define the following "deviation" patterns

$$\delta\Phi(\theta_\chi, s_\chi) = \Phi(\theta_\chi, s_\chi) - \Phi(\theta_\chi, s_\chi^*), \tag{2}$$

$$\delta\tilde{\Phi}(\theta_\chi, s_\chi|\theta_Z) = \tilde{\Phi}(\theta_\chi, s_\chi|\theta_Z, s_Z) - \tilde{\Phi}(\theta_\chi, s_\chi^*|\theta_Z, s_Z), \tag{3}$$

where s_χ^* is the reference threshold value set at 0.5 sd, and s_Z is set to have a constant value of 0.75 sd. The $\delta\Phi(\theta_\chi, s_\chi)$ and $\delta\tilde{\Phi}(\theta_\chi, s_\chi|\theta_Z)$ maps depict the deviation of composite anomalies due to the change in the amplitude threshold used to identify MJO episodes. In computing $\delta\Phi(\theta_\chi, s_\chi)$, this sensitivity to the choice of s_χ is determined by sampling MJO cycles with no consideration of the phase and amplitude of the WTP. On the contrary, specific phase and amplitude information on the WTP are incorporated in the $\delta\tilde{\Phi}(\theta_\chi, s_\chi|\theta_Z)$ patterns. Since the two terms on the rhs of Eq. (3) are based on the same θ_Z and s_Z, their difference would remove the influence of the contribution of the WTP features to the MJO + WTP composite to a certain extent. If no interaction occurs between the extratropical signals associated with MJO and WTP, the WTP contribution to the MJO + WTP patterns would be completely removed by computing the deviation pattern $\delta\tilde{\Phi}(\theta_\chi, s_\chi|\theta_Z)$ in Eq. (3). In this limit of full independence among the MJO- and WTP-related perturbations, the anomalies in the MJO + WTP composite would be a linear superposition of the features in the individual MJO and WTP patterns. Under this condition, and for given θ_χ and s_χ, the deviation patterns corresponding to different θ_Z categories would be similar to each other, and to the pattern $\delta\Phi(\theta_\chi, s_\chi)$ as obtained in Eq. (2).

Conversely, we could analyze the sensitivity of the WTP component to the choice of s_Z, by defining

$$\delta\Phi(\theta_Z, s_Z) = \Phi(\theta_Z, s_Z) - \Phi(\theta_Z, s_Z^*), \tag{4}$$

$$\delta\tilde{\Phi}(\theta_Z, s_Z|\theta_\chi) = \tilde{\Phi}(\theta_Z, s_Z|\theta_\chi, s_\chi) - \tilde{\Phi}(\theta_Z, s_Z^*|\theta_\chi, s_\chi), \tag{5}$$

where s_Z^* is the reference threshold value for the amplitude of WTP episodes (also set at 0.5 sd), and $s_\chi = 0.75$ sd. By applying similar reasoning as in the previous paragraph, independence between the MJO and WTP signals would lead to strong resemblance between patterns of $\delta\tilde{\Phi}(\theta_Z, s_Z|\theta_\chi)$ for various θ_χ categories, as well as between $\delta\tilde{\Phi}(\theta_Z, s_Z|\theta_\chi)$ and $\delta\Phi(\theta_Z, s_Z)$ for given θ_Z and s_Z.

As an illustration of the deviation patterns obtained in this analysis procedure, the distribution of $\delta\Phi(\theta_\chi = 8, s_\chi = 2.5$ sd) and $\delta\tilde{\Phi}(\theta_\chi = 8, s_\chi = 2.5$ sd$|\theta_Z = 8)$ are displayed in Fig. 13. There exits a strong spatial correspondence between these two charts. The spatial correlation coefficient between these two maps, as well as the rms amplitude of the individual patterns relative to their respective spatial mean, are computed for the domain of 30°–90°N, 120°E–90°W. The high correlation value (0.65) and the comparable rms amplitudes (~20 m for both patterns) offer quantitative evidence for the similarity between Figs. 13a,b. These patterns also bear considerable resemblance with those of $\delta\tilde{\Phi}(\theta_\chi = 8, s_\chi = 2.5$ sd$|\theta_Z)$ for other phase categories θ_Z ranging from 1 to 7 (not shown).

Parallel computations are performed using Eqs. (2)–(3) to obtain deviation patterns for different combinations of the phase categories θ_Z, θ_χ, and with s_χ varying from 0.75 to 2.5 sd in intervals of 0.25 sd. Similarly, deviation patterns are obtained using Eqs. (4)–(5) for different amplitude thresholds s_Z with the same range. Spatial resemblance between deviation patterns is quantitatively assessed using correlation coefficients and rms amplitudes. The results of this analysis are summarized in Fig. 14. The rms amplitudes of $\delta\Phi(\theta_\chi, s_\chi)$ and $\delta\tilde{\Phi}(\theta_\chi, s_\chi|\theta_Z)$ are plotted in Fig. 14a, for eight dis-

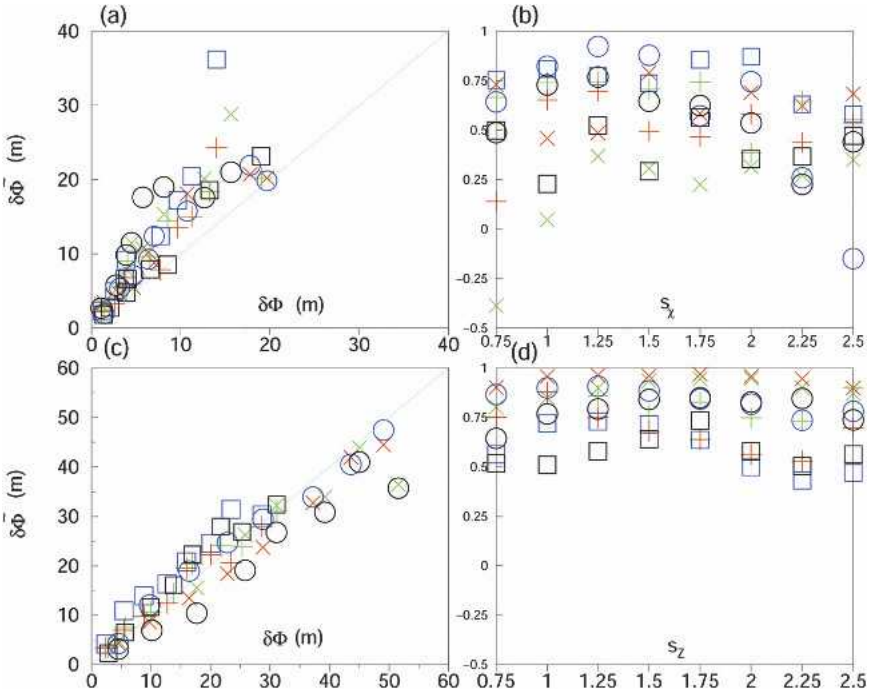

FIG. 14. (a) Scatterplot of rms amplitudes about the spatial average of $\delta\tilde{\Phi}(\theta_\chi, s_\chi|\theta_Z)$ vs those of $\delta\Phi(\theta_\chi, s_\chi)$ for eight different combinations of (θ_χ, θ_Z), and for s_χ varying from 0.75 to 2.5 sd. The diagonal line corresponds to the slope-1 line through the origin. (b) Spatial correlation coefficient between $\delta\tilde{\Phi}(\theta_\chi, s_\chi|\theta_Z)$ and $\delta\Phi(\theta_\chi, s_\chi)$ plotted as a function of s_χ, for the same combinations of phase categories considered in (a). (c) Same as in (a), but for amplitudes of $\delta\tilde{\Phi}(\theta_Z, s_Z|\theta_\chi)$ vs those of $\delta\Phi(\theta_Z, s_Z)$. (d) Same as in (b), but for correlation between $\delta\tilde{\Phi}(\theta_Z, s_Z|\theta_\chi)$ and $\delta\Phi(\theta_Z, s_Z)$. All rms and correlation statistics are based on model-simulated 300-mb data in the 30°–90°N, 120°E–90°W region. In all panels, data for a given phase combination of (θ_χ, θ_Z) are indicated using the same plotting symbol.

tinct combinations of (θ_χ, θ_Z),[7] and for various threshold of s_χ. The proximity of the data points to the slope-1 line indicates that the amplitudes of the deviation patterns obtained from Eqs. (2)–(3) are similar to each other. The pattern correlation values between the $\delta\Phi(\theta_\chi, s_\chi)$ and $\delta\tilde{\Phi}(\theta_\chi, s_\chi|\theta_Z)$ maps for the same set of phase categories are shown in Fig. 14b for various s_χ. The average pattern correlation for all data entries is 0.55. The $\delta\Phi(\theta_Z, s_Z)$ and $\delta\tilde{\Phi}(\theta_Z, s_Z|\theta_\chi)$ maps are compared in a similar manner in Figs. 14c,d. Again these patterns have similar rms amplitudes. The spatial correlation between these patterns is quite high, with an average value of 0.77. The statistics presented in Fig. 14 confirm that the MJO + WTP anomalies can be treated as the linear superposition of signals related to the MJO and WTP separately.

[7] They are phases (1, 1), (8, 8), (4, 4), (5, 5), (8, 1), (1, 8), (5, 4), and (4, 5). These are phase combinations that give rise to strong constructive interference between perturbations associated with the MJO and WTP.

7. Discussion and summary

The recurrent intraseasonal anomalies of the 300-mb height field in the vicinity of the key region in the North Pacific are studied, based on GCM simulations and data from NCEP–NCAR reanalyses. A substantial fraction of the year-to-year changes in intraseasonal activity over this region can be attributed to the SST variability in the Tropics. These prevalent circulation anomalies take the form of a wave train extending from the subtropical Pacific to North America, with a spatial structure that resembles the PNA pattern. In higher latitudes, the anomalies propagate westward. Wave activity diagnostics are used to depict the typical direction of wave dispersion and to unveil possible sources of activity for the intraseasonal anomalies. Wave activity is seen to originate from the subtropical western Pacific and northeast Asia during the development phase of the midlatidue circulation patterns. There is also southeastward dispersion from the principal anomaly center in the North Pacific. Based on GCM simulations, the anomalous extratropical features related to the MJO

and WTP are also studied individually. It is demonstrated that those features bear a considerable resemblance to certain regional aspects of the recurrent intraseasonal anomalies in the North Pacific–North American sector.

The impact of ENSO on intraseasonal activity in the North Pacific sector has been investigated. In general, activity is enhanced (suppressed) in the cold (warm) phase of ENSO. During cold events there is stronger incoming wave activity flux from the western Pacific in the development stage of the recurrent anomalies. There is also stronger dispersion from the North Pacific ridge to the west coast of the United States in the cold ENSO phase. Such a difference in the properties of the intraseasonal anomalies during warm and cold events is very similar to the ENSO modulation of the MJO-related circulation pattern in the extratropics. During cold events, the MJO is accompanied by a more stationary wave train, southeastward dispersion from the North Pacific is more prominent, and perturbations are stronger over the northwestern North American seaboard. During warm events there is a more obvious split of the wave dispersion pattern associated with the MJO, with one branch being directed toward the subtropical eastern Pacific and the other branch toward northern Canada. The modification of the waveguide properties of the Pacific jet by ENSO accounts for some of the differences in dispersion characteristics during warm and cold events. On the other hand, there is little change of the spatial structure of the circulation anomalies associated with WTP during opposite phases of ENSO.

The above results highlight the special role of the MJO in linking ENSO forcing in the Tropics to intraseasonal variability over the North Pacific. The MJO activity is more confined to the western Pacific during cold ENSO events as compared to warm events. The enhanced intraseasonal perturbations in the convective heating over the western Pacific lead to stronger Rossby wave propagation from that region in cold episodes (Fig. 5), with the subtropical portion of the PNA-like wave train being more anchored to the western Pacific (Figs. 5 and 8). Since the extratropical basic state and the forcing related to the MJO are both modulated by ENSO at the same time, further study is required to ascertain their relative importance in affecting the intraseasonal variability in the North Pacific. To address this issue, experiments using barotropic or baroclinic models with different mean flow structures and different MJO forcing (vorticity source or diabatic heating) could be conducted. Given that this type of experiment is sensitive to the choice of the background flow (see Ting and Sardeshmukh 1993), experimental results based on the GCM as well as the observational basic states should be examined.

Finally, the nature of the interactions between extratropical anomalies associated with the MJO and WTP is investigated. The MJO and WTP phenomena are found to be almost independent of each other. Multiple regression analysis reveals that they exert comparable influences on the intraseasonal activity over the midlatitude North Pacific. The extratropical circulation anomalies resulting from the joint occurrence of MJO and WTP are essentially a linear superposition of circulation anomalies associated with the MJO and WTP separately.

Nakamura et al. (1997) emphasized the importance of feedback from synoptic-scale eddies in maintaining blocking flows. The height tendency due to the convergence of vorticity fluxes associated with high-frequency eddies is computed, following Lau (1988). It is found that high-frequency activity tends to reinforce the recurrent intraseasonal circulation patterns (not shown). However, the magnitude of this feedback is only moderate. It should be pointed out that Nakamura et al. (1997) were interested in the strongest blocking events in their data record. On the other hand, the regression analysis used in this study would encompass a broader class of activity. Further work is required in order to delineate the relationship between the recurrent intraseasonal anomalies examined in our study and blocking episodes in the North Pacific.

It is also worth noting that the recurrent intraseasonal perturbations in the North Pacific exhibit a distinct westward tilt with increasing height (not shown). Further analysis based on wave activity diagnostics suggests that baroclinic processes could be important for the growth of perturbations. This result is consistent with the study of Black (1997). The baroclinicity of the wintertime basic state (as measured by the vertical wind shear at 700 mb) is stronger (weaker) during cold (warm) events over the high-latitude North Pacific. It is possible that the growth of intraseasonal anomalies is also influenced by ENSO through its effect on the baroclinicity of the basic state. This mechanism is noticeably different from the ENSO modulation of intraseasonal variability by altering the stability of the mean barotropic flow, as suggested by Palmer (1988).

Acknowledgments. We thank Isaac Held and Paul Kushner for their interest and encouragement throughout the course of this study, and John Lanzante for conducting the GCM integration used in this investigation. Suggestions from Klaus Weickmann and two reviewers helped to improve our paper.

APPENDIX A

Analysis of Variance

The results in Fig. 1c are obtained by the analysis of variance (ANOVA) method outlined in Rowell et al. (1995). Further discussion can be found in von Storch and Zwiers (2001).

Suppose a set of values $\eta_{i,j}$ is obtained from an ensemble GCM experiment with imposed interannually varying SST conditions, where $i = 1, 2, \ldots, N$ and $j = 1, 2, \ldots, M$. Here N is the number of years in the experiment and M is the number of ensemble integrations. The unbiased estimate of the internal variance is defined as

$$\mathrm{var}_{\mathrm{internal}} \equiv \frac{1}{(M-1)N}\sum_{j=1}^{M}\sum_{i=1}^{N}(\eta_{ij} - \{\eta\}_i)^2,$$

where

$$\{\eta\}_i = \frac{1}{M}\sum_{j=1}^{M}\eta_{ij}$$

is the ensemble mean of η for each year. The estimate of the external variance is given by

$$\mathrm{var}_{\mathrm{external}} \equiv \frac{1}{N-1}\sum_{i=1}^{N}(\{\eta\}_i - \{\overline{\eta}\})^2,$$

where

$$\{\overline{\eta}\} = \frac{1}{N}\sum_{i=1}^{N}\{\eta\}_i$$

is the mean of $\{\eta\}_i$ over all years. An estimate of the variance due to the varying SST common to all ensemble members can be found as

$$\mathrm{var}_{\mathrm{SST}} = \mathrm{var}_{\mathrm{external}} - \frac{1}{M}\mathrm{var}_{\mathrm{internal}}.$$

This step can be interpreted as removing the residual amount of variance due to the presence of internal variability (see Rowell et al. 1995). In practice $\mathrm{var}_{\mathrm{SST}}$ can be negative in some region. Its value is set to zero wherever this occurs.

The total variance is given by $\mathrm{var}_{\mathrm{total}} = \mathrm{var}_{\mathrm{SST}} + \mathrm{var}_{\mathrm{internal}}$, and the ratio $\mathrm{var}_{\mathrm{SST}}/\mathrm{var}_{\mathrm{total}}$ can be interpreted as the fraction of variance attributed to the SST variability. Figure 1c shows the square root of this ratio, based on the rms value η of the 10–60-day filtered 300-mb height field computed for each year.

APPENDIX B

Complex Empirical Orthogonal Functions

The space–time characteristics of the MJO and WTP cycle are identified in this study using eigenanalysis techniques. For the MJO, complex empirical orthogonal functions (CEOFs) of the 10–100-day bandpass-filtered 200-mb velocity potential are found (see, e.g., Horel 1984), based on data within the region of 20°N–20°S. Data were subsampled such that one out of every three grid points is selected in the longitudinal direction. For the WTP, CEOFs of the Z_{300} field are computed based on 10–45-day bandpass-filtered data and only values at selected grid points (based on an equal-area consideration) in the high-latitude region of 55°–90°N, 90°E–90°W are used. [The above methodology concerning the WTP, including the frequency cutoffs of the time filters, follows that used by Lau and Nath (1999), except that their domain of analysis extends farther south.] Data within the period of November–March are used in the eigenanalyses for both the MJO and the WTP. The leading CEOF of the velocity potential (Z_{300}) explains ~70% (35%) of the domain-integrated variance.

The real and imaginary parts of the first CEOF of the velocity potential, computed based on GCM data for all years, are shown in Fig. B1. The real and imaginary

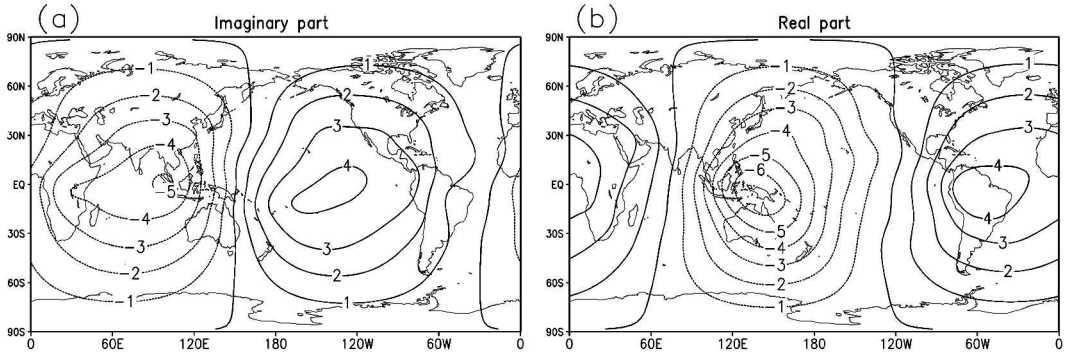

FIG. B1. (a) Imaginary and (b) real part of the first CEOF of the 10–100-day filtered velocity potential at 200 mb, for the Nov–Mar period. The patterns are found by regressing the velocity potential field upon the leading PC. Units: 10^6 m^2 s^{-1}. Computation is based on GCM data for all years.

eigenvector patterns, both having a wavenumber-1 structure, are in quadrature in space. The pattern for the real part (Fig. B1b) represents a large-scale 200-mb divergence anomaly over the western Pacific, and a convergence anomaly over South America. Similarly, the imaginary part of the eigenvector (Fig. B1a) indicates intense rising over the Indian Ocean, and sinking over the eastern Pacific. The real part and the imaginary part of the PC time series (not shown) are in temporal quadrature, with the imaginary part leading the real part. The PC together with its associated eigenvector patterns indicate that anomalies with a wavenumber-1 structure are propagating eastward. The eigenvector patterns for the reanalysis (not shown) are similar to those for the GCM. The spatial patterns for the leading CEOF of Z_{300} based on the GCM data are practically the same as the multiple regression coefficients shown in Figs. 12a,b.

REFERENCES

Anyamba, E. K., and B. C. Weare, 1995: Temporal variability of the 40–50-day oscillation in tropical convection. *Int. J. Climatol.,* **15,** 379–402.

Black, R. X., 1997: Deducing anomalous wave source regions during the life cycles of persistent flow anomalies. *J. Atmos. Sci.,* **54,** 895–907.

Branstator, G., 1987: A striking example of the atmosphere's leading traveling pattern. *J. Atmos. Sci.,* **44,** 2310–2323.

Broccoli, A. J., and S. Manabe, 1992: The effects of orography on midlatitude Northern Hemisphere dry climates. *J. Climate,* **5,** 1181–1201.

Chen, W. Y., and H. M. Van den Dool, 1997: Asymmetric impact of tropical SST anomalies on atmospheric internal variability over the North Pacific. *J. Atmos. Sci.,* **54,** 725–740.

Compo, G. P., P. D. Sardeshmukh, and C. Penland, 2001: Changes of subseasonal variability associated with El Niño. *J. Climate,* **14,** 3356–3374.

Dickson, R. R., and J. Namias, 1976: North American influences on the circulation and climate of the North Atlantic sector. *Mon. Wea. Rev.,* **104,** 1255–1265.

Dole, R. M., 1986: Persistent anomalies of the extratropical Northern Hemisphere wintertime circulation: Structure. *Mon. Wea. Rev.,* **114,** 178–207.

——, and N. D. Gordon, 1983: Persistent anomalies of the extratropical Northern Hemisphere wintertime circulation: Geographical distribution and regional persistence characteristics. *Mon. Wea. Rev.,* **111,** 1567–1586.

Fink, A., and P. Speth, 1997: Some potential forcing mechanisms of the year-to-year variability of the tropical convection and its intraseasonal (25–70-day) variability. *Int. J. Climatol.,* **17,** 1513–1534.

Gordon, C. T., and W. F. Stern, 1982: A description of the GFDL global spectral model. *Mon. Wea. Rev.,* **110,** 625–644.

Hendon, H. H., 2000: Impact of air–sea coupling on the Madden–Julian oscillation in a general circulation model. *J. Atmos. Sci.,* **57,** 3939–3952.

——, C. Zhang, and J. D. Glick, 1999: Interannual variation of the Madden–Julian oscillation during austral summer. *J. Climate,* **12,** 2538–2550.

Higgins, R. W., and K. C. Mo, 1997: Persistent North Pacific circulation anomalies and the tropical intraseasonal oscillation. *J. Climate,* **10,** 223–244.

Horel, J. D., 1984: Complex principal component analysis: Theory and examples. *J. Appl. Meteor.,* **23,** 1660–1673.

——, and J. M. Wallace, 1981: Planetary-scale atmospheric phenomena associated with the Southern Oscillation. *Mon. Wea. Rev.,* **109,** 813–829.

Hoskins, B. J., and T. Ambrizzi, 1993: Rossby wave propagation on a realistic longitudinally varying flow. *J. Atmos. Sci.,* **50,** 1661–1671.

Kalnay, E., and Coauthors, 1996: The NCEP/NCAR 40-Year Reanalysis Project. *Bull. Amer. Meteor. Soc.,* **77,** 437–471.

Kiladis, G. N., and K. M. Weickmann, 1992: Circulation anomalies associated with tropical convection during northern winter. *Mon. Wea. Rev.,* **120,** 1900–1923.

Knutson, T. R., and K. M. Weickmann, 1987: 30–60 day atmospheric oscillations: Composite life cycles of convection and circulation anomalies. *Mon. Wea. Rev.,* **115,** 1407–1436.

Kushnir, Y., 1987: Retrograding wintertime intraseasonal disturbances over the North Pacific Ocean. *J. Atmos. Sci.,* **44,** 2727–2742.

Kutzbach, J. E., 1970: Large-scale features of monthly mean Northern Hemisphere anomaly maps of sea-level pressure. *Mon. Wea. Rev.,* **98,** 708–716.

Lau, N.-C., 1988: Variability of the observed midlatitude storm tracks in relation to low-frequency changes in the circulation pattern. *J. Atmos. Sci.,* **45,** 2718–2743.

——, and M. J. Nath, 1996: The role of the "atmospheric bridge" in linking tropical Pacific ENSO events to extratropical SST anomalies. *J. Climate,* **9,** 2036–2057.

——, and ——, 1999: Observed and GCM-simulated westward-propagating, planetary-scale fluctuations with approximately three-week periods. *Mon. Wea. Rev.,* **127,** 2324–2345.

——, and ——, 2003: Atmosphere–ocean variations in the Indo-Pacific sector during ENSO episodes. *J. Climate,* **16,** 3–20.

Madden, R. A., and P. R. Julian, 1971: Detection of a 40–50 day oscillation in the zonal wind in the tropical Pacific. *J. Atmos. Sci.,* **28,** 702–708.

——, and ——, 1972: Description of global-scale circulation cells in the tropics with a 40–50 day period. *J. Atmos. Sci.,* **29,** 1109–1123.

Manabe, S., J. Smagorinsky, and R. F. Strickler, 1965: Simulated climatology of a general circulation model with a hydrological cycle. *Mon. Wea. Rev.,* **93,** 769–798.

Mullen, S. L., 1989: Model experiments on the impact of Pacific sea surface temperature anomalies on blocking frequency. *J. Climate,* **2,** 997–1013.

Nakamura, H., M. Nakamura, and J. L. Anderson, 1997: The role of high- and low-frequency dynamics in blocking formation. *Mon. Wea. Rev.,* **125,** 2074–2093.

Namias, J., 1978: Multiple causes of the North American abnormal winter 1976–77. *Mon. Wea. Rev.,* **106,** 279–295.

——, 1986: Persistence of flow patterns over North America and adjacent ocean sectors. *Mon. Wea. Rev.,* **114,** 1368–1383.

Naoe, H., Y. Matsuda, and H. Nakamura, 1997: Rossby wave propagation in idealized and realistic zonally varying flow. *J. Meteor. Soc. Japan,* **75,** 687–700.

Palmer, T. N., 1988: Medium and extended range predictability and stability of the Pacific/North America mode. *Quart. J. Roy. Meteor. Soc.,* **114,** 691–713.

Renwick, J. A., and J. M. Wallace, 1996: Relationships between

North Pacific wintertime blocking, El Niño, and the PNA pattern. *Mon. Wea. Rev.,* **124,** 2071–2076.

Rowell, D. P., C. K. Folland, K. Maskell, and M. N. Ward, 1995: Variability of summer rainfall over tropical north Africa (1906–92): Observations and modelling. *Quart. J. Roy. Meteor. Soc.,* **121,** 669–704.

Takaya, K., and H. Nakamura, 2001: A formulation of a phase-independent wave-activity flux for stationary and migratory quasigeostrophic eddies on a zonally varying basic flow. *J. Atmos. Sci.,* **58,** 608–627.

Tam, C.-Y., 2003: The impact of ENSO on tropical and extratropical atmospheric variability on intraseasonal and synoptic time scales as inferred from observations and GCM simulations. Ph.D. dissertation, Princeton University, 197 pp.

——, and N.-C. Lau, 2005: Modulation of the Madden–Julian oscillation by ENSO: Inferences from observations and GCM simulations. *J. Meteor. Soc. Japan,* in press.

Ting, M., and P. D. Sardeshmukh, 1993: Factors determining the extratropical response to equatorial diabatic heating anomalies. *J. Atmos. Sci.,* **50,** 907–918.

van Loon, H., and J. C. Rogers, 1978: The seesaw in winter temperatures between Greenland and northern Europe. Part I: General description. *Mon. Wea. Rev.,* **106,** 296–310.

Vincent, D. G., A. Fink, J. M. Schrage, and P. Speth, 1998: High- and low-frequency intraseasonal variance of OLR on annual and ENSO timescales. *J. Climate,* **11,** 968–986.

von Storch, H., and F. W. Zwiers, 2001: *Statistical Analysis in Climate Research.* Cambridge University Press, 484 pp.

Wallace, J. M., and D. S. Gutzler, 1981: Teleconnections in the geopotential height field during the Northern Hemisphere winter. *Mon. Wea. Rev.,* **109,** 784–812.